NANO LETTERS
Letter
Cite This: Nano Lett. 2018, 18, 5211−5216
pubs.acs.org/NanoLett

Charge Carrier Dynamics in Photocatalytic Hybrid Semiconductor−Metal Nanorods: Crossover from Auger Recombination to Charge Transfer

Yuval Ben-Shahar,[†] John P. Philbin,[§] Francesco Scotognella,[‡] Lucia Ganzer,[‡] Giulio Cerullo,*[,‡] Eran Rabani,*[,§,∥] and Uri Banin*[,†]

[†]The Institute of Chemistry and Center for Nanoscience and Nanotechnology, The Hebrew University of Jerusalem, Jerusalem 91904, Israel

[‡]IFN-CNR, Dipartimento di Fisica, Politecnico di Milano, Milan 20133, Italy

[§]Department of Chemistry, University of California and Lawrence Berkeley National Laboratory, Berkeley, California 94720-1460, United States

[∥]The Sackler Institute for Computational Molecular and Materials Science, Tel Aviv University, Tel Aviv, Israel 69978

Supporting Information

ABSTRACT: Hybrid semiconductor−metal nanoparticles (HNPs) manifest unique, synergistic electronic and optical properties as a result of combining semiconductor and metal physics via a controlled interface. These structures can exhibit spatial charge separation across the semiconductor−metal junction upon light absorption, enabling their use as photocatalysts. The combination of the photocatalytic activity of the metal domain with the ability to generate and accommodate multiple excitons in the semiconducting domain can lead to improved photocatalytic performance because injecting multiple charge carriers into the active catalytic sites can increase the quantum yield. Herein, we show a significant metal domain size dependence of the charge carrier dynamics as well as the photocatalytic hydrogen generation efficiencies under nonlinear excitation conditions. An understanding of this size dependence allows one to control the charge carrier dynamics following the absorption of light. Using a model hybrid semiconductor−metal CdS−Au nanorod system and combining transient absorption and hydrogen evolution kinetics, we reveal faster and more efficient charge separation and transfer under multiexciton excitation conditions for large metal domains compared to small ones. Theoretical modeling uncovers a competition between the kinetics of Auger recombination and charge separation. A crossover in the dominant process from Auger recombination to charge separation as the metal domain size increases allows for effective multiexciton dissociation and harvesting in large metal domain HNPs. This was also found to lead to relative improvement of their photocatalytic activity under nonlinear excitation conditions.

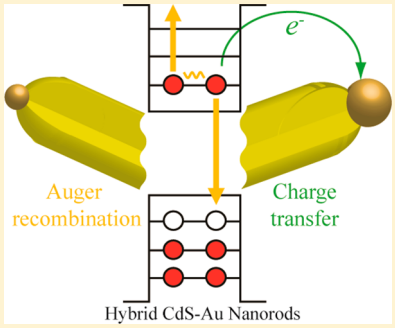

KEYWORDS: *Hybrid semiconductor−metal nanoparticles, multiexcitons, photocatalysis, hydrogen evolution*

Hybrid semiconductor−metal nanoparticles (HNPs) offer combined and synergistic photophysical and chemical properties.[1,2] One promising example that has many applications is that of light-induced charge separation. This process begins with light absorption by the semiconductor component, which creates an electron−hole pair (i.e., an exciton) on the semiconductor. Then, due to the band alignment across the semiconductor−metal interface, the electron undergoes ultrafast transfer to the metal domain while the hole is restricted to the semiconductor region. The resulting spatially separated charges can then each be harnessed for photocatalytic reactions. The discovery of this unique ability of HNPs sparked promise in utilizing HNPs as photocatalysts in various applications including solar to fuel conversion,[3] biomedical,[4,5] and photopolymerization[6] in 3D printing. The specific materials,[7−9] shapes,[10−12] sizes,[13−16] and surface ligands[17−19] used to make the HNPs have been shown to influence the charge carrier dynamics and, therefore, the overall photocatalytic performance.[20] Alongside the structural effects mentioned above, the reaction conditions have proven to have a significant impact on the photocatalytic efficiencies of such nanosystems.[21−24]

High-excitation fluences lead to the generation of multiple excitons (MX) on the semiconductor segment, as was reported previously for spherical,[25−27] rod,[28−30] and platelets[31] nanostructures. The formation of excess charge carriers that can be transferred to the catalytic site may lead to enhanced photocatalytic efficiency, especially in multielectron reactions such as hydrogen generation via water reduction or CO_2 reduction.[32,33] Hence, there is a need to better understand

Received: May 29, 2018
Revised: June 26, 2018
Published: July 9, 2018

DOI: 10.1021/acs.nanolett.8b02169
Nano Lett. 2018, 18, 5211−5216

MX dynamics in hybrid nanosystems (specifically with respect to charge separation and transfer).

Typically, MX dynamics in a semiconductor nanocrystal are governed by Auger recombination in which an electron−hole pair (exciton) recombines nonradiatively and transfers its energy to another exciton which then rapidly dissipates it, resulting in the effective annihilation of one exciton. Auger recombination lifetimes in nanomaterials have been shown to range from tens to hundreds of picoseconds[25] and to scale linearly with nanocrystal volume for both CdSe and PbSe spherical nanocrystals.[34,35] One way to tune the Auger recombination lifetime is via the shape of the nanoparticles. For example, elongated nanorods (NRs) exhibit longer Auger recombination lifetimes in comparison to spherical quantum dots (QDs).[29,30] An additional difference between NRs and QDs is that the Auger recombination rate as a function of the number of excitons, n, is proportional to $n(n-1)$ in NRs and on the contrary is proportional to $n^2(n-1)$ in QDs (i.e., Auger recombination is governed by exciton−exciton collisions in NRs and three-particle collisions in QDs).[30,36] The weaker dependence on n and the smaller biexciton binding energies[37] significantly extend the MX lifetimes in NRs compared to QDs with similar optical properties.

We recently reported a metal domain size effect on the photocatalytic hydrogen generation efficiency and charge carrier dynamics in semiconductor−metal CdS−Au HNPs.[13] Transient absorption (TA) measurements showed a monotonically increasing trend for the rate and efficiency of charge transfer from the semiconductor to the metal domain as the metal tip size of HNPs increases. The charge transfer time scale ranged from approximately a nanosecond for small-tipped CdS−Au HNPs to tens of picoseconds for relatively large-tipped CdS−Au HNPs. This trend was analyzed using Fermi's golden rule and ascribed chiefly to the scaling of the density of states of the metal domain. However, the fast charge transfer was found to be counteracted by a reduced water reduction activity due to insufficient overpotential in large-tipped HNPs. Thus, the interplay between the semiconductor to metal charge transfer and the actual water reduction resulted in a nonmonotonic metal domain size effect in which optimal performance was obtained by an intermediate metal domain size. Similar phenomena have been reported recently by other groups.[15,38−40]

Herein, we present metal domain size-dependent charge carrier dynamics that vary due to the excitation conditions, revealing the advantages of larger-tipped HNPs for photocatalytic water reduction and hydrogen generation under high energy fluences. Applying a combination of ultrafast TA spectroscopy, hydrogen generation yield studies, and computational modeling we observe and rationalize the competition between the Auger recombination, exciton dissociation, and charge carrier transfer to the metal tip.

We use as a model system hybrid semiconductor−metal CdS−Au NR structures. CdS NRs with lengths of 49.1 nm and diameters of 4.2 nm were synthesized by modifying a previously reported procedure that employs seeded growth[41] (see Supporting Information for details). After growing the CdS NRs, site-selective Au deposition on a single NR apex with high control of the metal tip size was obtained by following a recently reported procedure.[13] Specifically, following spontaneous metal nucleation in dark conditions to form site-selective small metal islands on the apexes of the CdS NRs, light-induced metal deposition at low temperature (2−4 °C) allowed the metal domain size to be controlled by varying the Au^{3+}/NRs molar ratio. The hybrid nanoparticles were then transferred to aqueous solution. The phase transfer was performed with polyethylenimine, which was reported as high-performance surface coating for photocatalytic applications and provides good colloidal stability.[17]

Figure 1 shows TEM images of CdS−Au HNPs with two different Au tip sizes, 1.5 ± 0.2 nm (Figure 1a) and 7.1 ± 0.8 nm (Figure 1b). Their corresponding absorption spectra are shown in Figure 1c. Both the CdS NRs and CdS−Au HNPs spectra exhibit a sharp rise at 460 nm, which arises from the onset of absorption of the CdS NRs. A slight blue shift of the first excitonic transition of the semiconductor segment in the L-HNPs is observed (~6 nm) which can be assigned to plasmon-exciton coupling[42,43] manifested more strongly for increased metal domain and a minor change in the CdS rod component diameter size distribution following metal growth. (Figure S2) Several additional absorption features are seen to the blue of the absorption onset that come from higher excited optical transitions of the CdS NRs, signifying the samples are monodisperse. A plasmon peak develops at 540 nm for the large-tipped HNPs.

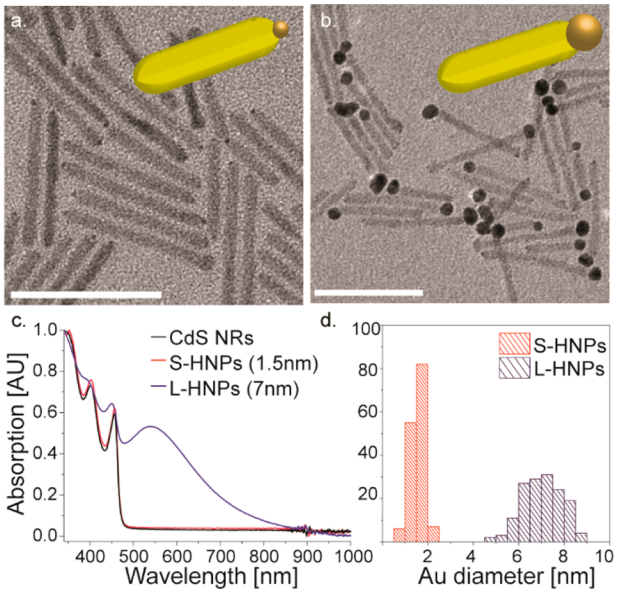

Figure 1. TEM images of (a) CdS−Au hybrid nanoparticles (49.1 nm × 4.2 nm, see Supporting Information and Figure S1 for more details) with a 1.5 ± 0.2 nm and (b) 7.1 ± 0.8 nm Au domain. Scale bars are 50 nm. (c) UV−vis absorbance spectra of CdS−Au hybrid nanoparticles showing the development of the plasmonic feature at ~540 nm as the Au tip size increases. (d) Size distribution histograms of the Au metal domain diameters.

Charge carrier dynamics were monitored via broadband ultrafast TA spectroscopy with 100 fs time resolution. All samples were measured under similar conditions (specifically, sample optical density, excitation wavelength, pump beam size, and ambient atmosphere) at different excitation fluences. Figure S3 shows a sequence of differential transmission ($\Delta T/T$) spectra of the bare CdS NRs at early times following a 400 nm optical excitation, which creates high energy electrons and holes. We observe rapid intraband relaxation of the electrons and holes to the lowest energy exciton levels (0.2−0.3 ps). This relaxation manifests itself by the instantaneous formation and the subsequent rapid decay of a negative peak at ~470 nm

DOI: 10.1021/acs.nanolett.8b02169
Nano Lett. 2018, 18, 5211−5216

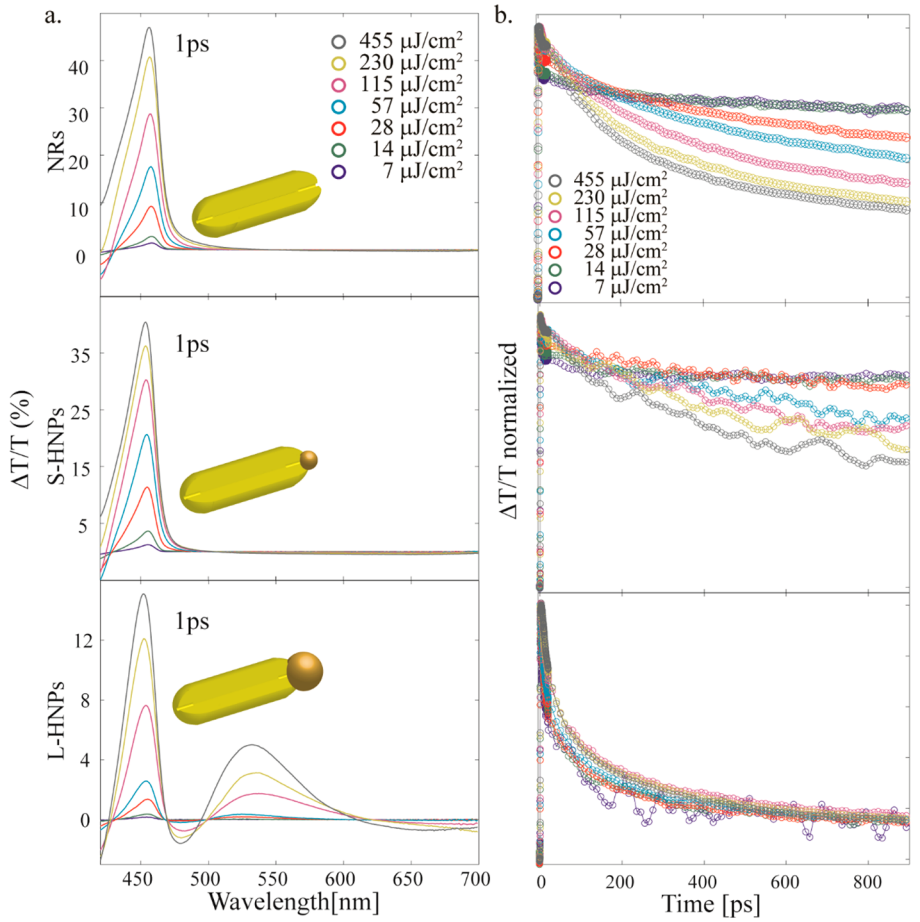

Figure 2. (a) $\Delta T/T$ spectra of CdS NRs and CdS−Au hybrid nanoparticles for different Au metal tip sizes including 1.5 nm (S-HNPs) and 7.1 nm (L-HNPs) under 400 nm excitation at different fluences after 1 ps. (b) Corresponding normalized dynamics of the bleach recovery at 450 nm, attributed to the first excitonic transition of the CdS NR component for CdS NRs and CdS−Au hybrid nanoparticles with different Au metal tip sizes.

in the $\Delta T/T$ spectrum, assigned to hot carriers absorption (Figure S3), along with the emergence of a pronounced bleach signal around 450 nm that is attributed to the depletion of the first excitonic transition in the CdS NRs due to electron state filling.[44] An additional higher-energy exciton transition feature (at ∼420 nm) arises during this relaxation process due to the interaction of the first excitonic transition with other exciton states.[45] Lastly, for the large Au-tipped HNPs a broad bleach feature develops at ∼540 nm, corresponding to the plasmonic feature of the Au domains.

Figure 2 presents $\Delta T/T$ spectra at 1 ps pump−probe delay for the CdS NRs and the HNPs with different Au tip sizes under different excitation fluences. At this delay, hot carrier relaxation to the band edge has completed and the subsequent bleach signal dynamics are dominated by the decay of the first excitonic transition due to electron−hole recombination (either radiative or nonradiative) in the case of NRs or by additional relaxation routes such as charge transfer to the metal domain for HNPs.[42] Indeed, the bleach signal for NRs under a low excitation fluence (7 $\mu J/cm^2$) shows only minor recovery within 1 ns (30%, Figure 2b upper panel) which suggests the dominance of the long-lived single exciton state. With increasing fluences, the amplitude of the bleach signal increases and is accompanied by both a blue shift and broadening of the peak as a result of the formation of additional excitons that occupy higher energy states, as apparent from the normalized spectra displayed in Figure S4.[46,47] At long delay times (>800 ps) for all fluences, due to the Auger decay process a single excitonic state is observed, as indicated by the merging of the bleach signal peak positions to the same energy (Figure S4).

The complete normalized bleach signal recovery dynamics up to 1 ns for CdS NRs and CdS−Au HNPs under a wide range of excitation fluences (7−455 $\mu J/cm^2$) are presented in Figure 2b. The bleach signal of the CdS NRs shows, as expected, faster decay dynamics with increased excitation fluence because Auger recombination dominates the decay for high fluences. A similar trend is observed for small metal-tipped HNPs; however, the effect is slightly diminished as seen by the lower decay rates and higher bleach amplitudes at longer time scales (1 ns). We postulate that the diminished decay observed at high fluences in small-tipped HNPs relative to CdS NRs is due to charge transfer of excited (i.e., hot) electrons in the semiconductor to the metal domain. This hot electron transfer reduces the population of the band-edge electrons after 1 ps, which results in a bleach recovery dynamics in the small-tipped HNPs similar to the one observed in NRs with a lower number of excitons initially formed. In contrast to the aforementioned fluence-dependent bleach signal dynamics of NRs and small-tipped HNPs, large-tipped HNPs do not reveal a significant power dependence—similar recovery rates are seen for all excitation fluences. The observed independent recovery rates indicate the presence of a

DOI: 10.1021/acs.nanolett.8b02169
Nano Lett. 2018, 18, 5211−5216

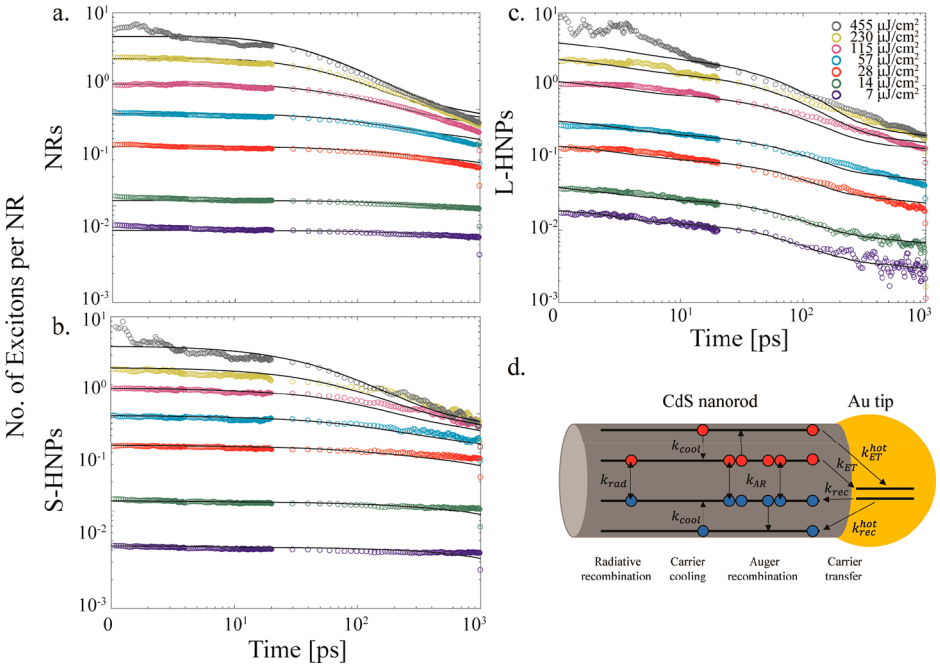

Figure 3. Experimental dynamics of number of excitons per rod for (a) CdS NRs and (b) small and (c) large metal-tipped CdS−Au hybrid nanoparticles at different fluences, alongside the fitted Markov chain Monte Carlo simulation curves (solid black lines). (d) A pictorial representation of the states and the four types of events that make up our kinetic model. Electrons are shown in red and holes in blue. Double-sided arrows indicate a loss of an exciton whereas single sided arrows indicate the carrier moving from one state to another.

faster relaxation route that does not scale according to typical Auger recombination processes and can be assigned to electron transfer from the semiconductor component to the metal domain, as was reported previously for CdS−Au HNPs with similar dimensions revealing similar typical recovery lifetimes.

We followed previously reported procedures in order to estimate the number of absorbed photons (i.e., the number of electron−holes initially created) per rod for each excitation fluence.[29,31,48,49] (see Supporting Information and Figure S5 for more details) Using this conversion procedure, which assumes that the number of excitons per rod obeys a Poisson distribution, we converted the measured $\Delta T/T$ dynamics to the average number of excitons per NR ($n(t)$) for each excitation fluence as a function of time (Figure 3). Note that due to the presence of the substantial plasmonic feature in the steady state absorption spectra for the large metal-tipped HNPs the contribution of the metal to the absorption cannot be ignored. As a simple approximation, the overall absorption can be considered as a sum of the absorption of the two individual components: the semiconductor NR and the metal tip.[50] Thus, within this approximation measurements of the ratios of Cd^+ ions between NRs, small-tipped HNPs, and large-tipped HNPs samples with the same optical density (as confirmed by inductively coupled plasma mass spectrometry, see Supporting Information for details) allow the extraction of a scaling factor for the absorbed photons/excitons per NR. For all systems, at early delay times a linear dependence of the TA bleach amplitudes with the excitation fluence was observed for $n(t = 0) < 1$. For higher values of $n(t = 0)$, the bleach amplitudes saturated due to the states becoming filled; specifically, a maximum of $n(t = 0) \approx 7$ was observed (Figure S6).

In order to rationalize the results, we have developed a model that explicitly disentangles the importance of radiative recombination, Auger recombination, and electron transfer in the three systems: CdS NRs, small-tipped CdS−Au HNPs, and large-tipped CdS−Au HNPs. Our model includes all the essential processes of charge dynamics in the HNPs: carrier cooling, radiative recombination, charge transfer (both hot and band-edge electron transfer and hole recombination) and Auger recombination (all processes are shown pictorially in Figure 3d). We solved the set of coupled differential equations (see Supporting Information for the full set of equations) by running trajectories with a Monte Carlo approach using the Gillespie algorithm.[51] The trajectories began by initializing the system with the experimentally determined number of hot electrons and holes created by the pump pulse. The kinetic model then allowed us to simulate the decay of the hot electrons and holes on the NR via the processes listed above. Because it is known how each process depends on the particles on the NR, we were able to fit a rate constant of each process. Specifically, the rate constant (i.e., base rate) of Auger recombination corresponds to the Auger recombination rate for $n = 2$, and the overall Auger recombination rate increases with the number of excitons with a scaling of $n(n - 1)/2$. See the Supporting Information for more details of the model and Table S1 for the fitted parameters.

The fitted curves in Figure 3 show the results of our Markov chain Monte Carlo simulations. The experimental data is well represented by the model. Note some deviations only at the highest fluences for the large-tipped HNPs. First, the additional fast decay component on a picosecond time scale at the highest fluence in this sample may be the result of direct excitation of the gold domain electrons through intraband transitions. Indeed gold NPs under high excitation conditions manifest picoseconds decay processes assigned to electron−phonon interactions.[52] In addition, for this metal domain size the simulated number of excitons at long delay times under the highest fluences overestimates the experimental signal. This overestimation is assigned to inaccuracies of the assumption

DOI: 10.1021/acs.nanolett.8b02169
Nano Lett. 2018, 18, 5211−5216

employed for evaluation of the average number of excitons per rod that considers a fixed fraction of direct excitation of the semiconductor component versus the metal tip while at the highest fluences this may change as the metal tip absorption contribution is not expected to show saturation.

Overall, considering the simplicity of the model it reproduces the experimental data remarkably well. For the CdS NRs, as expected, Auger recombination dominates the multiexcitonic decays. We found that a base biexciton Auger recombination rate constant of $(180\ \text{ps})^{-1}$ matches the experimental decays very well, and we used this base Auger recombination rate in our small and large-tipped HNP simulations as well.

For small-tipped HNPs, Auger recombination outcompetes electron transfer from the semiconductor to the metal tip. This is especially true for high fluences because the rate of Auger recombination increases the with square of the number of excitons (i.e., $k_{AR} \propto n(n-1)$) whereas electron transfer rate only scales linearly with the number of electrons. The smaller recovery amplitudes observed in comparison to bare NRs at 1 ns delay can be explained by a fast hot electron transfer (lifetime of ~2 ps) which lowers the excited electron populations remaining in the nanorod CB state.

On the other hand, for large-tipped HNPs electron transfer dominates (lifetimes of ~0.25 ps for hot electron transfer and ~44 ps for band-edge electron transfer). Almost no Auger recombination events occur in the large-tipped HNPs; thus, these simulations are consistent with the experimentally observed absence of fluence dependence of the MX decay in large-tipped HNPs. Altogether, these simulations point toward large-tipped HNPs benefiting more than small tips from absorbing multiple photons, because the large-tipped HNPs are able to extract all the excited electrons whereas the small-tipped HNPs lose most of their excited electrons due to Auger recombination.

To demonstrate the superior MX harvesting abilities of large Au domains relative to small Au domains under nonlinear excitation conditions, photocatalytic hydrogen generation measurements from water reduction were conducted under similar nonlinear excitation conditions to those used in the TA experiments. Figure 4 shows calculated quantum yields (QY) for small and large-tipped HNPs under different excitation fluences at 400 nm excitation wavelength (the intensities used in TA are marked in green dots). Excitation at this frequency, high above the band gap energy, guarantees the probability of generating more than biexcitons, as observed and predicted by both experimental and theoretical results above, respectively. In the linear regime, small-tipped HNPs exhibit better photocatalytic efficiency, as was previously reported;[13] however, increasing the excitation fluence raises the QY initially but eventually diminishes the QY of small-tipped HNPs due to the loss of excess excitation to the MX Auger recombination processes. The photocatalytic performance of large-tipped HNPs is significantly improved by applying nonlinear excitation conditions relative to the single exciton regime, because of the effective competition of the electron transfer with the MX Auger recombination rates. We note that eventually at the higher fluences the overall efficiency is decreased, given the optical saturation under higher fluence excitation conditions. The relative effect on the QY of large-tipped HNPs is born out further by plotting the QY ratio of small- versus large-tipped HNPs. The ratio decreases dramatically from 5:1 favoring hydrogen evolution from the small tips in the single exciton regime to close to 1:1 in the MX regime (Figure 4).

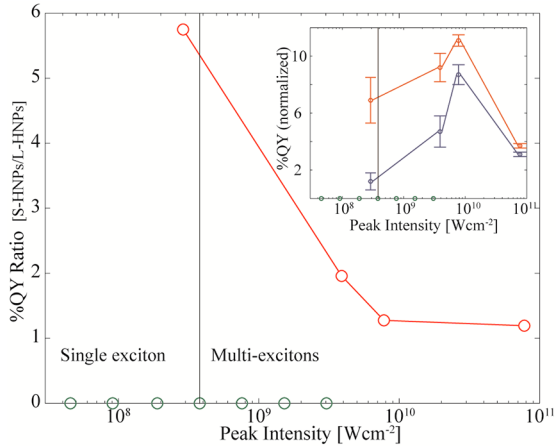

Figure 4. Hydrogen generation efficiencies ratio between small-tipped and large-tipped HNPs as a function of excitation fluence presented as peak intensity of the irradiation beam (red circles). Inset shows normalized hydrogen generation %QY of small-tipped HNPs (red circles with guideline) and large-tipped HNPs (blue circles and guideline) as a function of excitation fluences presented as peak intensity of the irradiation beam. Green circles mark the corresponding peak intensities used in the TA experiments.

In conclusion, CdS−Au HNPs with large Au tips are found to be advantageous for MX dissociation and transfer to the metal domain. This also led to relative improvement in their photocatalytic activity under nonlinear excitation conditions for the hydrogen generation reaction. This size dependence was explained by the competition between Auger recombination that dominates the MX dynamics in NRs and small-tipped HNPs and ultrafast charge transfer that is greatly enhanced and therefore dominates over Auger recombination in large-tipped HNPs. Altogether, an in-depth understanding of the synergistic light-induced charge separation process across the semiconductor−metal nanojunction in both the low and high excitation limits provides a key-knob to control the relaxation dynamics and will lead to the further utilization of hybrid metal−semiconductor nanosystems as efficient photocatalysts in numerous applications.

■ ASSOCIATED CONTENT

Supporting Information

The Supporting Information is available free of charge on the ACS Publications website at DOI: 10.1021/acs.nanolett.8b02169.

Experimental details, alongside TEM images and size distribution statistics of the used NRs for achieved HNPs. Complementary TA spectra and data analysis are presented followed by a detailed description of the presented modeling and fitting procedure (PDF)

■ AUTHOR INFORMATION

Corresponding Authors

*E-mail: Uri.Banin@mail.huji.ac.il.
*E-mail: Eran.Rabani@Berkeley.edu.
*E-mail: Giulio.Cerullo@polimi.it.

ORCID

Yuval Ben-Shahar: 0000-0001-9050-7005

DOI: 10.1021/acs.nanolett.8b02169
Nano Lett. 2018, 18, 5211−5216

John P. Philbin: 0000-0002-8779-0708
Uri Banin: 0000-0003-1698-2128

Notes

The authors declare no competing financial interest.

■ ACKNOWLEDGMENTS

We thank Professor Daniel Strasser's lab from the Institute of Chemistry, The Hebrew University of Jerusalem, for assistance in the photocatalysis measurements. The research leading to these results was supported in part by the Israel Science Foundation − Alternative Fuels Program Center of Excellence (Grant 1867/17). U.B. thanks the Alfred & Erica Larisch memorial chair. Y.B.S. acknowledges support by the Ministry of Science and Technology, Israel & The Camber Scholarship. E.R. acknowledges support from the UC Lab Fee Research Program (Grant LFR-17-477237). U.B. and G.C. acknowledge support from Horizon 2020 (654148, Laserlab-Europe).

■ REFERENCES

(1) Costi, R.; Saunders, A. E.; Banin, U. *Angew. Chem., Int. Ed.* **2010**, *49*, 4878−4897.
(2) Banin, U.; Ben-Shahar, Y.; Vinokurov, K. *Chem. Mater.* **2014**, *26*, 97−110.
(3) Wu, K.; Lian, T. *Chem. Soc. Rev.* **2016**, *45*, 3781−3810.
(4) Waiskopf, N.; Ben-Shahar, Y.; Galchenko, M.; Carmel, I.; Moshitzky, G.; Soreq, H.; Banin, U. *Nano Lett.* **2016**, *16*, 4266−4273.
(5) Fan, J.-X.; Liu, M.-D.; Li, C.-X.; Hong, S.; Zheng, D.-W.; Liu, X.-H.; Chen, S.; Cheng, H.; Zhang, X.-Z. *Nanoscale Horiz.* **2017**, *2*, 349−355.
(6) Pawar, A. A.; Halivni, S.; Waiskopf, N.; Ben-Shahar, Y.; Soreni-Harari, M.; Bergbreiter, S.; Banin, U.; Magdassi, S. *Nano Lett.* **2017**, *17*, 4497−4501.
(7) Aronovitch, E.; Kalisman, P.; Mangel, S.; Houben, L.; Amirav, L.; Bar-Sadan, M. *J. Phys. Chem. Lett.* **2015**, *6*, 3760−3764.
(8) Kalisman, P.; Houben, L.; Aronovitch, E.; Kauffmann, Y.; Bar-Sadan, M.; Amirav, L. *J. Mater. Chem. A* **2015**, *3*, 19679−19682.
(9) Choi, J. Y.; Jeong, D.; Lee, S. J.; Kang, D.-G.; Kim, S. K.; Nam, K. M.; Song, H. *Nano Lett.* **2017**, *17*, 5688−5694.
(10) Bang, J. U.; Lee, S. J.; Jang, J. S.; Choi, W.; Song, H. *J. Phys. Chem. Lett.* **2012**, *3*, 3781−3785.
(11) Simon, T.; Carlson, M. T.; Stolarczyk, J. K.; Feldmann, J. *ACS Energy Lett.* **2016**, *1*, 1137−1142.
(12) Nakibli, Y.; Kalisman, P.; Amirav, L. *J. Phys. Chem. Lett.* **2015**, *6*, 2265−2268.
(13) Ben-Shahar, Y.; Scotognella, F.; Kriegel, I.; Moretti, L.; Cerullo, G.; Rabani, E.; Banin, U. *Nat. Commun.* **2016**, *7*, 10413.
(14) Schweinberger, F. F.; Berr, M. J.; Döblinger, M.; Wolff, C.; Sanwald, K. E.; Crampton, A. S.; Ridge, C. J.; Jäckel, F.; Feldmann, J.; Tschurl, M.; Heiz, U. *J. Am. Chem. Soc.* **2013**, *135*, 13262−13265.
(15) Karakus, M.; Sung, Y.; Wang, H. I.; Mics, Z. Z.; Char, K.; Bonn, M.; Caovas, E.; Cánovas, E. *J. Phys. Chem. C* **2017**, *121*, 13070−13077.
(16) Amirav, L.; Alivisatos, A. P. *J. Phys. Chem. Lett.* **2010**, *1*, 1051−1054.
(17) Ben-Shahar, Y.; Scotognella, F.; Waiskopf, N.; Kriegel, I.; Dal Conte, S.; Cerullo, G.; Banin, U. *Small* **2015**, *11*, 462−471.
(18) Wang, P.; Zhang, J.; He, H.; Xu, X.; Jin, Y. *Nanoscale* **2015**, *7*, 5767−5775.
(19) Wilker, M. B.; Utterback, J. K.; Greene, S.; Brown, K. A.; Mulder, D. W.; King, P. W.; Dukovic, G. *J. Phys. Chem. C* **2018**, *122*, 741−750.
(20) Ben-Shahar, Y.; Banin, U. *Top. Curr. Chem.* **2016**, *374*, 54.
(21) Simon, T.; Bouchonville, N.; Berr, M. J.; Vaneski, A.; Adrović, A.; Volbers, D.; Wyrwich, R.; Döblinger, M.; Susha, A. S.; Rogach, A. L.; Jäckel, F.; Stolarczyk, J. K.; Feldmann, J. *Nat. Mater.* **2014**, *13*, 1013−1018.
(22) Berr, M. J.; Wagner, P.; Fischbach, S.; Vaneski, A.; Schneider, J.; Susha, A. S.; Rogach, A. L.; Jäckel, F.; Feldmann, J.; Jäckel, F.; Feldmann, J.; Jäckel, F.; Feldmann, J. *Appl. Phys. Lett.* **2012**, *100*, 223903.
(23) Berr, M. J.; Vaneski, A.; Mauser, C.; Fischbach, S.; Susha, A. S.; Rogach, A. L.; Jäckel, F.; Feldmann, J.; Jaeckel, F.; Feldmann, J. *Small* **2012**, *8*, 291−297.
(24) Wu, K.; Chen, Z.; Lv, H.; Zhu, H.; Hill, C. L.; Lian, T. *J. Am. Chem. Soc.* **2014**, *136*, 7708−7716.
(25) Oron, D.; Kazes, M.; Banin, U. *Phys. Rev. B: Condens. Matter Mater. Phys.* **2007**, *75*, 035330.
(26) Huang, J.; Huang, Z.; Yang, Y.; Zhu, H.; Lian, T. *J. Am. Chem. Soc.* **2010**, *132*, 4858−4864.
(27) Klimov, V. I. *Science (Washington, DC, U. S.)* **2000**, *287*, 1011−1013.
(28) Sitt, A.; Sala, F. D.; Menagen, G.; Banin, U. *Nano Lett.* **2009**, *9*, 3470−3476.
(29) Zhu, H.; Lian, T. *J. Am. Chem. Soc.* **2012**, *134*, 11289−11297.
(30) Aerts, M.; Spoor, F. C. M.; Grozema, F. C.; Houtepen, A. J.; Schins, J. M.; Siebbeles, L. D. A. *Nano Lett.* **2013**, *13*, 4380−4386.
(31) Li, Q.; Lian, T. *Nano Lett.* **2017**, *17*, 3152−3158.
(32) Roy, S. C.; Varghese, O. K.; Paulose, M.; Grimes, C. A. *ACS Nano* **2010**, *4*, 1259−1278.
(33) Manzi, A.; Simon, T.; Sonnleitner, C.; Doblinger, M.; Wyrwich, R.; Stern, O.; Stolarczyk, J. K.; Feldmann, J. *J. Am. Chem. Soc.* **2015**, *137*, 14007−14010.
(34) Klimov, V. I.; McGuire, J. A.; Schaller, R. D.; Rupasov, V. I. *Phys. Rev. B: Condens. Matter Mater. Phys.* **2008**, *77*, 195324.
(35) Schaller, R. D.; Klimov, V. I. *Phys. Rev. Lett.* **2004**, *92*, 186601.
(36) Htoon, H.; Hollingsworth, J. A.; Dickerson, R.; Klimov, V. I. *Phys. Rev. Lett.* **2003**, *91*, 227401.
(37) Oron, D.; Kazes, M.; Shweky, I.; Banin, U. *Phys. Rev. B: Condens. Matter Mater. Phys.* **2006**, *74*, 115333.
(38) Okuhata, T.; Kobayashi, Y.; Nonoguchi, Y.; Kawai, T.; Tamai, N. *J. Phys. Chem. C* **2015**, *119*, 2113−2120.
(39) Sagarzazu, G.; Inoue, K.; Saruyama, M.; Sakamoto, M.; Teranishi, T.; Masuo, S.; Tamai, N. *Phys. Chem. Chem. Phys.* **2013**, *15*, 2141.
(40) Nakibli, Y.; Mazal, Y.; Dubi, Y.; Wächtler, M.; Amirav, L. *Nano Lett.* **2018**, *18*, 357−364.
(41) Carbone, L.; Nobile, C.; De Giorgi, M.; Sala, F. D.; Morello, G.; Pompa, P.; Hytch, M.; Snoeck, E.; Fiore, A.; Franchini, I. R.; Nadasan, M.; Silvestre, A. F.; Chiodo, L.; Kudera, S.; Cingolani, R.; Krahne, R.; Manna, L. *Nano Lett.* **2007**, *7*, 2942−2950.
(42) Wu, K. F.; Rodriguez-Cordoba, W. E.; Yang, Y.; Lian, T. Q. *Nano Lett.* **2013**, *13*, 5255−5263.
(43) Dana, J.; Maity, P.; Ghosh, H. N. *Nanoscale* **2017**, *9*, 9723−9731.
(44) Wu, K. F.; Zhu, H. M.; Liu, Z.; Rodriguez-Cordoba, W.; Lian, T. Q.; Rodríguez-Córdoba, W.; Lian, T. Q. *J. Am. Chem. Soc.* **2012**, *134*, 10337−10340.
(45) Sacra, A.; Norris, D. J.; Murray, C. B.; Bawendi, M. G. *J. Chem. Phys.* **1995**, *103*, 5236−5245.
(46) Katz, D.; Wizansky, T.; Millo, O.; Rothenberg, E.; Mokari, T.; Banin, U. *Phys. Rev. Lett.* **2002**, *89*, 086801.
(47) Shabaev, A.; Efros, A. L. *Nano Lett.* **2004**, *4*, 1821−1825.
(48) Zhu, H.; Song, N.; Rodríguez-Córdoba, W.; Lian, T. *J. Am. Chem. Soc.* **2012**, *134*, 4250−4257.
(49) Trinh, M. T.; Houtepen, A. J.; Schins, J. M.; Hanrath, T.; Piris, J.; Knulst, W.; Goossens, A. P. L. M.; Siebbeles, L. D. A. *Nano Lett.* **2008**, *8*, 1713−1718.
(50) Shaviv, E.; Schubert, O.; Alves-Santos, M.; Goldoni, G.; Di Felice, R.; Vallée, F.; Del Fatti, N.; Banin, U.; Sönnichsen, C. *ACS Nano* **2011**, *5*, 4712−4719.
(51) Gillespie, D. T. *J. Phys. Chem.* **1977**, *81*, 2340−2361.
(52) Link, S.; El-Sayed, M. A. *J. Phys. Chem. B* **1999**, *103*, 8410−8426.

DOI: 10.1021/acs.nanolett.8b02169
Nano Lett. 2018, 18, 5211−5216